Fermi National Accelerator Laboratory

FERMILAB-Pub-93/017-E
CDF

Measurement of the Dijet Mass Distribution in $p\bar{p}$ Collisions at $\sqrt{s} = 1.8$ TeV

F. Abe et al
The CDF Collaboration

Fermi National Accelerator Laboratory
P.O. Box 500, Batavia, Illinois 60510

February 1993

Submitted to *Physical Review D*

Operated by Universities Research Association Inc. under Contract No. DE-AC02-76CHO3000 with the United States Department of Energy

Disclaimer

CDF/ANAL/JET/PUBLIC/1818
FERMILAB-PUB-93/017-E

Measurement of the Dijet Mass Distribution in $p\bar{p}$ Collisions at $\sqrt{s} = 1.8$ TeV

F. Abe,[12] M. Albrow,[6] D. Amidei,[15] C. Anway-Wiese,[3] G. Apollinari,[23] M. Atac,[6] P. Auchincloss,[22] P. Azzi,[17] A. R. Baden,[8] N. Bacchetta,[16] W. Badgett,[15] M. W. Bailey,[21] A. Bamberger,[6,a] P. de Barbaro,[22] A. Barbaro-Galtieri,[13] V. E. Barnes,[21] B. A. Barnett,[11] G. Bauer,[14] T. Baumann,[8] F. Bedeschi,[20] S. Behrends,[2] S. Belforte,[20] G. Bellettini,[20] J. Bellinger,[28] D. Benjamin,[27] J. Benlloch,[14] J. Bensinger,[2] A. Beretvas,[6] J. P. Berge,[6] S. Bertolucci,[7] K. Biery,[10] S. Bhadra,[9] M. Binkley,[6] D. Bisello,[17] R. Blair,[1] C. Blocker,[2] A. Bodek,[22] V. Bolognesi,[20] A. W. Booth,[6] C. Boswell,[11] G. Brandenburg,[8] D. Brown,[8] E. Buckley-Geer,[6] H. S. Budd,[22] G. Busetto,[17] A. Byon-Wagner,[6] K. L. Byrum,[1] C. Campagnari,[6] M. Campbell,[15] A. Caner,[6] R. Carey,[8] W. Carithers,[13] D. Carlsmith,[28] J. T. Carroll,[6] R. Cashmore,[6,a] A. Castro,[17] F. Cervelli,[20] K. Chadwick,[6] J. Chapman,[15] G. Chiarelli,[7] W. Chinowsky,[13] S. Cihangir,[6] A. G. Clark,[6] M. Cobal,[20] D. Connor,[18] M. Contreras,[4] J. Cooper,[6] M. Cordelli,[7] D. Crane,[6] J. D. Cunningham,[2] C. Day,[6] F. DeJongh,[6] S. Dell'Agnello,[20] M. Dell'Orso,[20] L. Demortier,[23] B. Denby,[6] P. F. Derwent,[15] T. Devlin,[24] D. DiBitonto,[25] M. Dickson,[22] R. B. Drucker,[13] K. Einsweiler,[13] J. E. Elias,[6] R. Ely,[13] S. Eno,[4] S. Errede,[9] A. Etchegoyen,[6,a] B. Farhat,[14] M. Frautschi,[16] G. J. Feldman,[8] B. Flaugher,[6] G. W. Foster,[6] M. Franklin,[8] J. Freeman,[6] H. Frisch,[4] T. Fuess,[6] Y. Fukui,[12] A. F. Garfinkel,[21] A. Gauthier,[9] S. Geer,[6] D. W. Gerdes,[15] P. Giannetti,[20]

Submitted to Physical Review D, February 16, 1993.

N. Giokaris,[23] P. Giromini,[7] L. Gladney,[18] M. Gold,[16] J. Gonzalez,[18] K. Goulianos,[23] H. Grassmann,[17] G. M. Grieco,[20] R. Grindley,[10] C. Grosso-Pilcher,[4] C. Haber,[13] S. R. Hahn,[6] R. Handler,[28] K. Hara,[26] B. Harral,[18] R. M. Harris,[6] S. A. Hauger,[5] J. Hauser,[3] C. Hawk,[24] T. Hessing,[25] R. Hollebeek,[18] A. Hölscher,[10] S. Hong,[15] G. Houk,[18] P. Hu,[19] B. Hubbard,[13] B. T. Huffman,[19] R. Hughes,[22] P. Hurst,[8] J. Huth,[6] J. Hylen,[6] M. Incagli,[20] T. Ino,[26] H. Iso,[26] H. Jensen,[6] C. P. Jessop,[8] R. P. Johnson,[6] U. Joshi,[6] R. W. Kadel,[13] T. Kamon,[25] S. Kanda,[26] D. A. Kardelis,[9] I. Karliner,[9] E. Kearns,[8] L. Keeble,[25] R. Kephart,[6] P. Kesten,[2] R. M. Keup,[9] H. Keutelian,[6] D. Kim,[6] S. B. Kim,[15] S. H. Kim,[26] Y. K. Kim,[13] L. Kirsch,[2] K. Kondo,[26] J. Konigsberg,[8] K. Kordas,[10] E. Kovacs,[6] M. Krasberg,[15] S. E. Kuhlmann,[1] E. Kuns,[24] A. T. Laasanen,[21] S. Lammel,[3] J. I. Lamoureux,[28] S. Leone,[20] J. D. Lewis,[6] W. Li,[1] P. Limon,[6] M. Lindgren,[3] T. M. Liss,[9] N. Lockyer,[18] M. Loreti,[17] E. H. Low,[18] D. Lucchesi,[20] C. B. Luchini,[9] P. Lukens,[6] P. Maas,[28] K. Maeshima,[6] M. Mangano,[20] J. P. Marriner,[6] M. Mariotti,[20] R. Markeloff,[28] L. A. Markosky,[28] J. Matthews,[16] R. Mattingly,[2] P. McIntyre,[25] A. Menzione,[20] E. Meschi,[20] T. Meyer,[25] S. Mikamo,[12] M. Miller,[4] T. Mimashi,[26] S. Miscetti,[7] M. Mishina,[12] S. Miyashita,[26] Y. Morita,[26] S. Moulding,[2] J. Mueller,[24] A. Mukherjee,[6] T. Muller,[3] L. F. Nakae,[2] I. Nakano,[26] C. Nelson,[6] D. Neuberger,[3] C. Newman-Holmes,[6] J. S. T. Ng,[8] M. Ninomiya,[26] L. Nodulman,[1] S. Ogawa,[26] R. Paoletti,[20] V. Papadimitriou,[6] A. Para,[6] E. Pare,[8] S. Park,[6] J. Patrick,[6] G. Pauletta,[20] L. Pescara,[17] G. Piacentino,[20] T. J. Phillips,[5] F. Ptohos,[8] R. Plunkett,[6] L. Pondrom,[28] J. Proudfoot,[1] G. Punzi,[20] D. Quarrie,[6] K. Ragan,[10] G. Redlinger,[4] J. Rhoades,[28] M. Roach,[27]

F. Rimondi,[6,a] L. Ristori,[20] W. J. Robertson,[5] T. Rodrigo,[6] T. Rohaly,[18] A. Roodman,[4] W. K. Sakumoto,[22] A. Sansoni,[7] R. D. Sard,[9] A. Savoy-Navarro,[6] V. Scarpine,[9] P. Schlabach,[8], E. E. Schmidt,[6] O. Schneider,[13] M. H. Schub,[21] R. Schwitters,[8] G. Sciacca,[20] A. Scribano,[20] S. Segler,[6] S. Seidel,[16] Y. Seiya,[26] G. Sganos,[10] M. Shapiro,[13] N. M. Shaw,[21] M. Sheaff,[28] M. Shochet,[4] J. Siegrist,[13] A. Sill,[22] P. Sinervo,[10] J. Skarha,[11] K. Sliwa,[27] D. A. Smith,[20] F. D. Snider,[11] L. Song,[6] T. Song,[15] M. Spahn,[13] A. Spies,[11] P. Sphicas,[14] R. St. Denis,[8] L. Stanco,[6,a] A. Stefanini,[20] G. Sullivan,[4] K. Sumorok,[14] R. L. Swartz, Jr.,[9] M. Takano,[26] K. Takikawa,[26] S. Tarem,[2] F. Tartarelli,[20] S. Tether,[14] D. Theriot,[6] M. Timko,[27] P. Tipton,[22] S. Tkaczyk,[6] A. Tollestrup,[6] J. Tonnison,[21] W. Trischuk,[8] Y. Tsay,[4] J. Tseng,[11] N. Turini,[20] F. Ukegawa,[26] D. Underwood,[1] S. Vejcik, III,[15] R. Vidal,[6] R. G. Wagner,[1] R. L. Wagner,[6] N. Wainer,[6] R. C. Walker,[22] J. Walsh,[18] G. Watts,[22] T. Watts,[24] R. Webb,[25] C. Wendt,[28] H. Wenzel,[20] W. C. Wester, III,[13] T. Westhusing,[9] S. N. White,[23] A. B. Wicklund,[1] E. Wicklund,[6] H. H. Williams,[18] B. L. Winer,[22] J. Wolinski,[25] D. Y. Wu,[15] X. Wu,[20] J. Wyss,[17] A. Yagil,[6] K. Yasuoka,[26] Y. Ye,[10] G. P. Yeh,[6] C. Yi,[18] J. Yoh,[6] M. Yokoyama,[26] J. C. Yun,[6] A. Zanetti,[20] F. Zetti,[20] S. Zhang,[15] W. Zhang,[17] S. Zucchelli,[6,a]

The CDF Collaboration

[1] *Argonne National Laboratory, Argonne, Illinois 60439*

[2] *Brandeis University, Waltham, Massachusetts 02254*

[3] *University of California at Los Angeles, Los Angeles, California 90024*

[4] *University of Chicago, Chicago, Illinois 60637*

(5) *Duke University, Durham, North Carolina 27706*

(6) *Fermi National Accelerator Laboratory, Batavia, Illinois 60510*

(7) *Laboratori Nazionali di Frascati, Istituto Nazionale di Fisica Nucleare, Frascati, Italy*

(8) *Harvard University, Cambridge, Massachusetts 02138*

(9) *University of Illinois, Urbana, Illinois 61801*

(10) *Institute of Particle Physics, Canada*

(11) *The Johns Hopkins University, Baltimore, Maryland 21218*

(12) *National Laboratory for High Energy Physics (KEK), Japan*

(13) *Lawrence Berkeley Laboratory, Berkeley, California 94720*

(14) *Massachusetts Institute of Technology, Cambridge, Massachusetts 02139*

(15) *University of Michigan, Ann Arbor, Michigan 48109*

(16) *University of New Mexico, Albuquerque, New Mexico 87131*

(17) *Universita di Padova, Instituto Nazionale di Fisica Nucleare, Sezione di Padova, I-35131 Padova, Italy*

(18) *University of Pennsylvania, Philadelphia, Pennsylvania 19104*

(19) *University of Pittsburgh, Pittsburgh, Pennsylvania 15260*

(20) *Istituto Nazionale di Fisica Nucleare, University and Scuola Normale Superiore of Pisa, I-56100 Pisa, Italy*

(21) *Purdue University, West Lafayette, Indiana 47907*

(22) *University of Rochester, Rochester, New York 14627*

(23) *Rockefeller University, New York, New York 10021*

(24) *Rutgers University, Piscataway, New Jersey 08854*

(25) *Texas A&M University, College Station, Texas 77843*

(26) *University of Tsukuba, Tsukuba, Ibaraki 305, Japan*

(27) *Tufts University, Medford, Massachusetts 02155*

(28) *University of Wisconsin, Madison, Wisconsin 53706*

Abstract

The dijet invariant mass distribution has been measured in the region between 120 and 1000 GeV/c^2, in 1.8 TeV $p\bar{p}$ collisions. The data sample was collected with the Collider Detector at Fermilab (CDF). Data are compared to leading order (LO) and next-to-leading order (NLO) QCD calculations using two different clustering cone radii R in the jet definition. A quantitative test shows good agreement of data with the LO and NLO QCD predictions for a cone of R = 1. The test using a cone of R = 0.7 shows less agreement. The NLO calculation shows an improvement compared to LO in reproducing the shape of the spectrum for both radii, and approximately predicts the cone size dependence of the cross section.

PACS numbers: 13.87.Ce, 12.38.Qk, 13.85.Ni

Hard scattering processes in high energy hadron-hadron collisions are dominated by events with most of the central hadronic activity concentrated in two jets. These events provide a testing ground for perturbative quantum chromo-dynamics (QCD), which at leading order (LO) describes two-body to two-body processes.

In this paper we present the differential production cross section as a function of the invariant mass of the two leading jets in the process $p\bar{p} \rightarrow jet + jet + X$ at a center of mass energy $\sqrt{s} = 1.8$ TeV. The data are based on an integrated luminosity of 4.2 pb^{-1} recorded by CDF [1] during the 1988-1989 run at the Fermilab Tevatron Collider. Previous studies reported by UA1 [2] and UA2 [3] at $\sqrt{s} = 540$ GeV, and by CDF [4] at $\sqrt{s} = 1.8$ TeV, with an integrated luminosity of 26 nb^{-1} show that the data agree with the LO QCD calculations. High statistics data from the 1988-1989 run, however, allow for more precise tests of QCD.

The description of events with more than two jets requires higher order calculations that should account, at the parton level, for the radiation which can occur from the initial and final state partons. Recently, next-to-leading order (NLO) calculations and experimental comparisons have become available for the inclusive jet cross section [5, 6] and for inclusive two-jet production [7, 8]. These calculations also allow perturbative QCD to be tested by reproducing the jet internal structure. An encouraging result is the qualitative agreement of the NLO calculation with the measurement of the transverse jet shape [9] at energies sufficiently high that hadronization effects are negligible.

Precise comparisons between measurements by different detectors, as well as between theoretical predictions and measurements, requires a common convention of jet definition, applicable to both experimental data and theoretical predictions. We reconstructed jets using a fixed-cone clustering algorithm [10, 11] with cone radius R $= \sqrt{\Delta\eta^2 + \Delta\phi^2}$, where $\eta = -ln[tan(\theta/2)]$ is the pseudorapidity, ϕ is the azimuthal angle (in radians) and θ is the polar angle with respect to the proton beam direction. The true jet energy (E) and momentum ($\mathbf{p}$) are defined as the total energy and momentum of all the particles (leptons, photons, and hadrons) emerging from the primary vertex within a cone of fixed radius R around the cluster centroid. For each event the number and the characteristics of the jets, seen as energy clusters in the experiment and as single partons or parton clusters in the calculation, depend on the cone radius. Jets appearing as separate clusters with a certain cone size may be merged together by a larger cone, and the cross section will change accordingly. In general, measurements or calculations of jet cross sections require that the jet cone size be explicitly specified. For example, the cone size dependence of the inclusive jet

cross section has been studied theoretically and experimentally [5, 6]. In this paper, we report measurements of dijet mass with R = 1.0 and R = 0.7.

The data are based on information from the CDF central calorimeter ($|\eta| \leq 1.1$) [12] which is composed of projective towers of scintillator-absorber sandwich construction, segmented in $\Delta\eta \times \Delta\phi = 0.1 \times 15°$. The data were collected using three single-jet online triggers, which required at least one cluster of transverse energy $E_T = Esin\theta$ greater than thresholds of 20, 40, or 60 GeV. The 20 and 40 GeV jet triggers were prescaled by factors of 300 and 30 respectively, to avoid saturation of the data acquisition bandwidth.

The uncorrected energy of a jet is defined by the clustering algorithm [11] as the scalar sum of the measured energies in the electromagnetic and hadronic compartments within a cone around the cluster centroid. The momentum of the cluster is calculated by assuming that the energy in each calorimeter tower belonging to the cluster is deposited by a massless particle hitting the center of the tower.

The measured energy and momentum of each jet were corrected, on average, for detector effects: degradation of the measurement due to calorimeter non-linearity, uninstrumented regions of the detector and bending of charged particle tracks in the CDF 1.4 T solenoid magnetic field in the central region. These corrections are based on a Monte Carlo study with a full detector simulation. The Monte Carlo program is tuned to reproduce (a) the charged particle fragmentation of jets observed in the data and (b) the calorimeter response to single charged pions and electrons (measured in a test beam) and to single isolated charged particles in the data from $p\bar{p}$ collisions. No attempt is made to reconstruct the energy of the parton from which the jet originates, e.g. no corrections are applied to account for energy lost out of the clustering cone

or to account for the soft component of the $p\bar{p}$ interaction (underlying event). Our energy scale corrections are intended to produce an unbiased estimate of the true jet 4-momentum $(E, \mathbf{p})$, defined above.

Events are selected by requiring: (a) the event vertex along the beam line to be within 60 cm of the center of the detector, and (b) the two leading jet axes (i.e., those with the highest transverse energies) to be in the pseudorapidity ranges $|\eta_1|, |\eta_2| < 0.7$. This assures that the jets are well contained in the central calorimeter.

We define $M_{jj}^{obs} = \sqrt{(E_1 + E_2)^2 - (\mathbf{p}_1 + \mathbf{p}_2)^2}$ which is the measured mass of the system composed by the two leading jets mentioned above. Here E_i and $\mathbf{p}_i$ (i = 1 or 2) are corrected energies and momenta of the two leading jets. Any remaining jets, produced largely by radiation from the initial and final states of the hard parton process, are not taken into account in the computation of M_{jj}^{obs}.

We combine the data from the three different online triggers by requiring that the measured dijet mass be large enough to be free of biases introduced by the trigger thresholds. For the cone radii R = 0.7 and R = 1.0 the mass thresholds above which our data selection is fully efficient are, respectively 120, 160, 240 GeV/c^2 and 140, 180 and 280 GeV/c^2 for samples which passed each of the three triggers. The observed differential cross section $d\sigma/dM_{jj}^{obs}$, integrated over the pseudorapidity intervals $|\eta_1|, |\eta_2| < 0.7$ and averaged over the mass bins, is listed in Table 1 for the cone radius R = 1.0 and in Table 2 for the cone radius R = 0.7. In these Tables, M_{jj}^{obs} is taken to be the center of each mass bin. The cross section, obtained from the number of events and the integrated luminosity [13], is corrected for the efficiency (94.3 %) of the 60 cm vertex cut. No corrections are necessary for the other selection cuts.

The major sources of systematic error on the measurement of the cross section come from uncertainties in the integrated luminosity, in the calorimeter response, and in the fragmentation tuning. The uncertainty in the integrated luminosity is 6.8% [13] . The uncertainty in the calorimeter response to hadrons arises from several sources. For hadron momenta below 10 GeV/c, the response is determined using the *in situ* calibration by charged particles in $p\bar{p}$ data, whose dominant uncertainty is the subtraction of energy from accompanying π^0's. At higher pion momenta, systematic effects come from uncertainty in the response across the face of the calorimeter and response in cracks between calorimeter cells. These are uninstrumented regions located at $\theta = 90°$ (where the two halves of the central calorimeter come together) and at the boundaries between calorimeter modules in the ϕ coordinate (ϕ cracks). The errors on the cross section due to the uncertainties in the calorimeter response and fragmentation tuning were estimated with the Monte Carlo by varying the simulation parameters within their uncertainties and looking at the effects on the measured cross sections. In particular, fragmentation was studied by comparing different versions of the HERWIG [14] fragmentation scheme. Tables 3 and 4 show the size of the main contributions to the systematic uncertainty in the cross section as a function of M_{jj}^{obs} for cone sizes of 1.0 and 0.7, respectively.

Tables 3 and 4 also show theoretical uncertainties in the LO QCD predictions. These arise from the following effects contributing to the jet 4-momenta but not accounted for by the LO calculations: the underlying event, parton shower products falling outside of the clustering cone and the presence of additional jets from higher order processes. We estimated the size of these effects from the data. The uncertainties from the underlying event energy and from energy falling outside the cone were

estimated by observing the amount of energy deposited at large angular separations from the nearest cluster in a sample of dijet events. The uncertainty due to events with additional jets at large angles, which are not generated by a LO diagram, was estimated by considering the influence on the observed M_{jj} distribution of an additional cut on the azimuthal separation of the two leading jets, requiring them to be "back to back" within an angle of 30°. The effect is small compared to the other uncertainties.

For each contribution, i.e. each column in Tables 3 and 4, the errors on the cross sections at different masses are completely correlated, i.e. $\rho_{ij} = \delta_{ij}/(\delta_i\delta_j) = 1$ for the correlation factor ρ between two mass bins i, j in terms of the variances δ^2. This allows one to calculate the covariance matrix from knowledge of the diagonal terms δ_i, δ_j: $\delta_{ij} = \delta_i\delta_j$. Different contributions, considered statistically independent from each other, can then be summed in quadrature: $\Delta_i^2 = \Sigma\delta_i^2$ and $\Delta_{ij} = \Sigma\delta_{ij}$, where Δ_i^2 is the variance for bin i and Δ_{ij} is the covariance for bins i, j. The "systematic uncertainties" and "theoretical uncertainties" shown in Tables 1 and 2 are respectively the sums in quadrature of all the different experimental and theoretical contributions.

The M_{jj}^{obs} spectrum differs from the true spectrum because of the finite M_{jj} resolution, which smears the distribution and changes its shape. We define the smearing function $g(t, M_{jj})$ as the probability density function of making a measurement error $t = M_{jj}^{obs} - M_{jj}$, thereby observing a mass M_{jj}^{obs} for a given true mass M_{jj}. Comparing a theoretically predicted M_{jj} spectrum to the observed one requires knowledge of the smearing function $g(t, M_{jj})$.

The smearing function depends on the clustering cone radius R. We estimate the smearing functions for different cone radii using a Monte Carlo simulation. The

event generator used in this Monte Carlo was HERWIG version 3.2 [14], whose jet fragmentation [15] and global event topological properties [16] were checked with the data. To smooth the statistical fluctuations of the Monte Carlo and to give a compact description of the smearing function, we use an analytic approximation of the function $g(t, M_{jj})$. For this purpose we assumed a parametric form for the function and determined the best parameter values by fitting the simulated data. The parametric form may be chosen freely, provided it fits the simulation well. We give below the parametrization of the smearing functions used in this analysis for the cone radius R = 1.0 and R = 0.7. The smearing function $g(t, M_{jj})$ is represented by a convolution of a Gaussian distribution with a truncated exponential:

$$g(t, M_{jj}) = \int \frac{1}{\alpha_1(M_{jj})} e^{\frac{y-\alpha_3(M_{jj})}{\alpha_1(M_{jj})}} \theta[\alpha_3(M_{jj}) - y] \frac{1}{\alpha_2(M_{jj})\sqrt{2\pi}} e^{\frac{-(t-y)^2}{2\alpha_2^2(M_{jj})}} dy$$

where

$$\theta[\alpha_3 - y] = \begin{cases} 0, & \text{if } y > \alpha_3; \\ 1, & \text{if } y < \alpha_3. \end{cases}$$

This combination reproduces the asymmetric tails due to losses in the calorimeter. The parameters α_1, α_2, and α_3 may be associated respectively with the "characteristic length" of the exponential tail, the standard deviation of the Gaussian fluctuations and the mass scale "offset". Each parameter is a linear combination of eight different functions of the true mass M_{jj}: $\alpha_i(M_{jj}) = \sum_k p_{ik}\gamma_k(M_{jj})$, $k = 1, ..., 8$. The functions $\gamma_k(M_{jj})$ and the coefficients p_{ik}, obtained by the fitting procedure on simulated data, are shown in Table 5. At large masses the parameter α_1, dominated by $\gamma_5(M_{jj})$, grows showing the increasing importance of asymmetric losses. The parameter α_2 has a substantial contribution from the function $\gamma_7(M_{jj})$ that behaves as $\sqrt{M_{jj}}$ for large M_{jj}, as expected for the mass dependence of sampling fluctuations in jet energy

measurements. All the other $\gamma_k(M_{jj})$ functions provide corrections to guarantee a good description of the $\alpha_i(M_{jj})$ parameters for a very large range of masses ($50 < M_{jj} < 1800$ GeV/c^2).

The smearing function described above was used to obtain the corrected differential cross section $d\sigma/dM_{jj}$ by deconvolution of the observed one. To unfold the cross section we chose the following parametric function of the dijet mass: $f(M_{jj}) = aM_{jj}^{-b}e^{-cM_{jj}}$, where a, b, and c are parameters to be determined. We folded it with the smearing function and we fit the folded function $f'(M_{jj}^{obs}) = \int f(M_{jj})\, g(t, M_{jj})\, dM_{jj}$ to the observed M_{jj}^{obs} spectrum. The best fit parameters a, b, c are shown in Table 6. The corrected cross section described by the fit parametric function $f(M_{jj})$ is an absolute differential cross section that can be compared to theoretical calculations without any knowledge of the detector details. However, it is valid only if the theoretical prediction being tested is well described by the parametrization $f(M_{jj}) = aM_{jj}^{-b}e^{-cM_{jj}}$, since the unfolding procedure requires as input this hypothesis on the shape of the M_{jj} spectrum. For instance, possible resonances [17], broadened by the finite resolution, cannot be recovered by the unfolding procedure. In the case of resonances, theoretical models should be checked by folding the predicted cross sections with appropriate smearing functions before comparing them to the observed M_{jj}^{obs} spectrum. All comparisons in this paper follow this technique.

Figures 1 and 2 show plots of the M_{jj}^{obs} spectrum observed with cone radii R=1.0 and R=0.7, respectively. The vertical error bars on the data points represent the statistical errors and the M_{jj}^{obs}-dependent part of the systematic errors combined in quadrature. The solid lines in each figure define a band of uncertainty in the LO theoretical predictions. To obtain these bands we varied the renormalization scale μ

in the range $p_T/2 < \mu < 2p_T$, using recent parametrizations for the proton structure functions (HMRS[18], MT[19], DFLM[20]). Each prediction was first folded with the smearing function appropriate to the cone radius in use, and then binned as in the data; the bands are the envelopes of all the folded predictions. The comparisons are made on an absolute scale. The theoretical predictions are lower than the data. The ratios of the data to the predictions range from a factor 1.5 (HMRSB, $\mu = p_T/2$) to a factor 3.6 (MT B2, $\mu = 2p_T$) for a cone size of 1.0. For a cone size of 0.7 the ratios are smaller, ranging from a factor 0.9 (HMRSB, $\mu = p_T/2$) to a factor 2.2 (MT B2, $\mu = 2p_T$). These discrepancies can be ascribed to the absence in the calculations of orders higher than $O(\alpha_s^2)$. The dotted lines in Figs. 1 and 2 show the NLO predictions calculated with the structure function HMRSB and the renormalization scale $\mu = AM_{jj}/2cosh(B\eta^*)$ [7], where $A = 0.5$, $B = 0.7$ and $\eta^* = |\eta_1 - \eta_2|/2$. The ratios of the data to the predictions are 1.10 for the larger cone size and 0.91 for the smaller one. Compared to the LO case, the ratio for the larger cone size is substantially reduced by the α_s^3 calculation which reproduces qualitatively the cone size dependence of the cross section. This dependence is described in Fig. 3 which shows the bin by bin ratio of the two spectra $(d\sigma_{R=1}/dM_{jj}^{obs})/(d\sigma_{R=0.7}/dM_{jj}^{obs})$. The error bars on the data points represent the statistical errors and the systematic errors combined in quadrature. We show only diagonal elements of the covariance matrix in the figure. Figure 3 also shows the ratios provided by the NLO calculations, with the structure functions HMRSB and MTS1 and with the following choices for the renormalization scale $\mu = AM_{jj}/2cosh(B\eta^*)$: A=0.25 (dotted lines), A=0.5 (solid lines), A=1 (dashed lines). Smaller values of the coefficient A predict a higher ratio, closer to the data. The dependence of the ratio on the structure functions is negligible.

We have made a more quantitative test of LO QCD by fitting our data to the various theoretical predictions obtained by changing structure functions and renormalization scale. In addition to the structure functions used to produce the bands in Figs. 1 and 2, we also tested older parametrizations (EHLQ[21], DO[22]). Since both data and theory have a normalization uncertainty, the free parameter of the fits was a global normalization factor. The LO confidence levels for measurements with both R = 0.7 and R = 1.0 are summarized in Table 7. These confidence levels take into account Poisson fluctuations of the bin contents, the absence of events with $M_{jj}^{obs} > 1000$ GeV/c^2, the systematic errors on the data, and their bin-to-bin correlations. The measurement with R = 1.0 agrees with the LO QCD calculations with all structure functions and various μ scales. However, the data and LO QCD seem to be in poor agreement when R = 0.7 is used.

We have performed the same test for the NLO prediction using the two structure functions HMRSB and MTS1 and varying the coefficient A of the renormalization scale $\mu = AM_{jj}/2cosh(0.7\eta^*)$. All confidence levels shown in Table 8 are better than the corresponding LO values.

A representative comparison of the data and theory is shown in Fig. 4. The M_{jj} spectra are compared to the best fit using the quantity $(data - fit)/fit$. The best fit, used as a reference (horizontal line), is the parametric function $f(M_{jj}) = aM_{jj}^{-b}e^{-cM_{jj}}$ folded with the detector resolution corresponding to the cone size in use and fit to the data (see Table 6). The error bars on the data points represent the statistical uncertainties only. The deviations $((QCD - fit)/fit)$ from the best fit of LO (solid lines) and NLO (dotted lines) theoretical predictions are also shown. The QCD predictions are obtained using the structure function MTS1 (showing the

best agreement with data) and all the renormalization scales shown in the Tables 7 and 8. All the theories have been fit to the data, allowing for a free normalization factor. The shape of the spectrum is almost independent of renormalization scale, but depends on the order of the calculation. In Fig. 4 the shapes predicted by the NLO calculations agree with both spectra better than the LO predictions (as expected from Tables 7 and 8). The improvement is more evident for the smaller cone, for which the radiation out of cone is more important. Figure 5 shows the same comparison between QCD predictions and data, using the structure function HMRSB. For this structure function we observe a smaller deviation between LO and NLO predictions.

We thank the Fermilab Accelerator Division, the Computer Division, and the CDF technical staff for their dedicated effort that made this experiment possible. This work was supported by the U.S. Department of Energy and the National Science Foundation; the Italian Istituto Nazionale di Fisica Nucleare; the Ministry of Science, Culture and Education of Japan; the Natural Sciences and Engineering Research Council of Canada; and the A.P. Sloan Foundation.

References

[1] F. Abe *et al.* (CDF Collaboration), Nucl. Instr. Meth. A **271**, 387 (1988).

[2] C. Albajar *et al.* (UA1 Collaboration), Phys. Lett. B **209**, 127 (1988).

[3] J. Alitti *et al.* (UA2 Collaboration), Z. Phys. C **49**, 17 (1991).

[4] F. Abe *et al.* (CDF Collaboration), Phys. Rev. D **41**, 1722 (1990).

[5] S. Ellis, Z. Kunszt and D. Soper, Phys. Rev. D **40**, 2188 (1989); Phys. Rev. Lett. **64**, 2121 (1990); F. Aversa *et al.*, Phys. Lett. B **210**, 225 (1988).

[6] F. Abe *et al.*, Phys. Rev. Lett. **68**, 1104 (1992).

[7] S. D. Ellis, Z. Kunszt, D. E. Soper, Phys. Rev. Lett. **69**, 1496 (1992).

[8] F. Abe *et al.*, Phys. Rev. Lett. **69**, 2896 (1992).

[9] F. Abe *et al.*, Phys. Rev. Lett. **70**, 713 (1993).

[10] J. Huth *et al.*, Fermilab Preprint Fermilab-Conf-90/249-E, Proceed. of the Summer Study on High Energy Physics (1990), Snowmass, Colorado.

[11] F. Abe *et al.*, Phys. Rev. D **45**, 1448 (1992).

[12] L. Balka *et al.*, Nucl. Instr. Meth. A **267**, 272 (1988); S. Bertolucci *et al.*, Nucl. Instr. Meth. A **267**, 301 (1988).

[13] F. Abe *et al.*, Phys. Rev. D **44**, 29 (1991).

[14] G. Marchesini and B. Webber, Nucl. Phys. B **310**, 461 (1988).

[15] F. Abe *et al.*, Phys. Rev. Lett. **65**, 968 (1990).

[16] Emilio Meschi, Laurea thesis, University of Pisa (1991).

[17] P. Frampton and S. Glashow, Phys. Lett. B **190**, 157 (1987).

[18] P. Harriman *et al.*, Phys. Rev. D **42**, 798 (1990).

[19] J. Morfin and W. Tung, Z. Phys. C **52**, 13 (1991).

[20] M. Diemoz *et al.*, Z. Phys. C **39**, 21 (1988).

[21] E. Eichten *et al.*, Rev. Mod. Phys. **56**, 579 (1984).

[22] D. Duke and J. Owens, Phys. Rev. D **30**, 49 (1984).

M_{jj}^{obs} GeV/c^2	$d\sigma/dM_{jj}^{obs}$ nb/(GeV/c^2)	Statistical uncertainty	Systematic uncertainty	Theoretical uncertainty
145	1.07×10^{0}	0.89×10^{-1}	0.36×10^{0}	0.39×10^{0}
155	7.82×10^{-1}	0.76×10^{-1}	0.25×10^{0}	0.27×10^{0}
165	5.14×10^{-1}	0.62×10^{-1}	0.18×10^{0}	0.18×10^{0}
175	4.39×10^{-1}	0.57×10^{-1}	0.13×10^{0}	0.13×10^{0}
185	2.85×10^{-1}	0.14×10^{-1}	0.92×10^{-1}	0.91×10^{-1}
195	2.36×10^{-1}	0.13×10^{-1}	0.69×10^{-1}	0.66×10^{-1}
205	1.56×10^{-1}	0.10×10^{-1}	0.51×10^{-1}	0.48×10^{-1}
215	1.31×10^{-1}	0.94×10^{-2}	0.39×10^{-1}	0.35×10^{-1}
225	9.64×10^{-2}	0.81×10^{-2}	0.30×10^{-1}	0.26×10^{-1}
235	7.35×10^{-2}	0.70×10^{-2}	0.23×10^{-1}	0.20×10^{-1}
245	5.05×10^{-2}	0.58×10^{-2}	0.18×10^{-1}	0.15×10^{-1}
255	4.11×10^{-2}	0.53×10^{-2}	0.14×10^{-1}	0.11×10^{-1}
265	4.11×10^{-2}	0.53×10^{-2}	0.11×10^{-1}	0.88×10^{-2}
275	2.16×10^{-2}	0.38×10^{-2}	0.93×10^{-2}	0.68×10^{-2}
285	2.12×10^{-2}	0.74×10^{-3}	0.75×10^{-2}	0.53×10^{-2}
295	1.86×10^{-2}	0.69×10^{-3}	0.61×10^{-2}	0.42×10^{-2}
305	1.43×10^{-2}	0.60×10^{-3}	0.50×10^{-2}	0.33×10^{-2}
315	1.24×10^{-2}	0.56×10^{-3}	0.41×10^{-2}	0.26×10^{-2}
325	1.00×10^{-2}	0.51×10^{-3}	0.34×10^{-2}	0.21×10^{-2}
335	7.97×10^{-3}	0.45×10^{-3}	0.28×10^{-2}	0.17×10^{-2}
345	6.52×10^{-3}	0.41×10^{-3}	0.23×10^{-2}	0.13×10^{-2}
355	5.83×10^{-3}	0.39×10^{-3}	0.20×10^{-2}	0.11×10^{-2}
365	5.16×10^{-3}	0.36×10^{-3}	0.17×10^{-2}	0.87×10^{-3}
375	4.32×10^{-3}	0.33×10^{-3}	0.14×10^{-2}	0.71×10^{-3}
385	3.48×10^{-3}	0.30×10^{-3}	0.12×10^{-2}	0.58×10^{-3}
395	3.02×10^{-3}	0.28×10^{-3}	0.10×10^{-2}	0.48×10^{-3}
410	2.10×10^{-3}	0.16×10^{-3}	0.81×10^{-3}	0.36×10^{-3}
430	1.58×10^{-3}	0.14×10^{-3}	0.60×10^{-3}	0.25×10^{-3}
450	1.19×10^{-3}	0.12×10^{-3}	0.44×10^{-3}	0.17×10^{-3}
480	6.84×10^{-4}	0.66×10^{-4}	0.29×10^{-3}	0.10×10^{-3}
520	3.32×10^{-4}	0.46×10^{-4}	0.17×10^{-3}	0.55×10^{-4}
560	1.79×10^{-4}	0.34×10^{-4}	0.10×10^{-3}	0.30×10^{-4}
600	9.58×10^{-5}	0.25×10^{-4}	0.63×10^{-4}	0.17×10^{-4}
660	7.03×10^{-5}	0.15×10^{-4}	0.32×10^{-4}	0.84×10^{-5}
740	2.88×10^{-5}	0.96×10^{-5}	0.13×10^{-4}	0.33×10^{-5}
820	6.39×10^{-6}	4.50×10^{-6}	0.59×10^{-5}	0.14×10^{-5}
930	5.48×10^{-6}	3.20×10^{-6}	0.22×10^{-5}	0.50×10^{-6}

Table 1: The observed differential cross section for a jet clustering cone size R=1.0. The cross sections are averaged over the mass bins and the M_{jj}^{obs} column on the left indicates the bin center. The theoretical uncertainty includes only the effect of the out of cone losses, the underlying event energy and the contribution from multi-jet events. Details of uncertainties are in Table 3.

M_{jj}^{obs} GeV/c^2	$d\sigma/dM_{jj}^{obs}$ nb/(GeV/c^2)	Statistical uncertainty	Systematic uncertainty	Theoretical uncertainty
125	1.46×10^{0}	0.10×10^{0}	0.49×10^{0}	0.47×10^{0}
135	9.56×10^{-1}	0.85×10^{-1}	0.33×10^{0}	0.30×10^{0}
145	5.83×10^{-1}	0.66×10^{-1}	0.22×10^{0}	0.20×10^{0}
155	3.96×10^{-1}	0.54×10^{-1}	0.16×10^{0}	0.13×10^{0}
165	3.04×10^{-1}	0.14×10^{-1}	0.11×10^{0}	0.91×10^{-1}
175	2.48×10^{-1}	0.13×10^{-1}	0.83×10^{-1}	0.64×10^{-1}
185	1.79×10^{-1}	0.11×10^{-1}	0.62×10^{-1}	0.45×10^{-1}
195	1.34×10^{-1}	0.93×10^{-2}	0.46×10^{-1}	0.32×10^{-1}
205	1.04×10^{-1}	0.82×10^{-2}	0.35×10^{-1}	0.24×10^{-1}
215	8.60×10^{-2}	0.75×10^{-2}	0.27×10^{-1}	0.17×10^{-1}
225	4.49×10^{-2}	0.54×10^{-2}	0.21×10^{-1}	0.13×10^{-1}
235	4.56×10^{-2}	0.54×10^{-2}	0.17×10^{-1}	0.96×10^{-2}
245	3.56×10^{-2}	0.95×10^{-3}	0.13×10^{-1}	0.73×10^{-2}
255	2.74×10^{-2}	0.84×10^{-3}	0.11×10^{-1}	0.56×10^{-2}
265	2.28×10^{-2}	0.76×10^{-3}	0.84×10^{-2}	0.43×10^{-2}
275	1.78×10^{-2}	0.67×10^{-3}	0.69×10^{-2}	0.33×10^{-2}
285	1.50×10^{-2}	0.62×10^{-3}	0.56×10^{-2}	0.26×10^{-2}
295	1.26×10^{-2}	0.57×10^{-3}	0.45×10^{-2}	0.20×10^{-2}
305	9.81×10^{-3}	0.50×10^{-3}	0.37×10^{-2}	0.16×10^{-2}
315	7.92×10^{-3}	0.45×10^{-3}	0.31×10^{-2}	0.12×10^{-2}
325	5.80×10^{-3}	0.39×10^{-3}	0.26×10^{-2}	0.99×10^{-3}
335	6.03×10^{-3}	0.39×10^{-3}	0.21×10^{-2}	0.79×10^{-3}
345	4.52×10^{-3}	0.34×10^{-3}	0.18×10^{-2}	0.64×10^{-3}
355	4.19×10^{-3}	0.33×10^{-3}	0.15×10^{-2}	0.51×10^{-3}
365	3.32×10^{-3}	0.29×10^{-3}	0.13×10^{-2}	0.42×10^{-3}
375	2.99×10^{-3}	0.28×10^{-3}	0.11×10^{-2}	0.34×10^{-3}
385	2.40×10^{-3}	0.25×10^{-3}	0.90×10^{-3}	0.28×10^{-3}
395	1.43×10^{-3}	0.19×10^{-3}	0.77×10^{-3}	0.23×10^{-3}
410	1.69×10^{-3}	0.15×10^{-3}	0.61×10^{-3}	0.17×10^{-3}
430	1.16×10^{-3}	0.12×10^{-3}	0.45×10^{-3}	0.12×10^{-3}
450	7.16×10^{-4}	0.96×10^{-4}	0.33×10^{-3}	0.85×10^{-4}
480	4.54×10^{-4}	0.54×10^{-4}	0.22×10^{-3}	0.52×10^{-3}
520	2.94×10^{-4}	0.43×10^{-4}	0.13×10^{-3}	0.28×10^{-4}
560	8.94×10^{-5}	0.24×10^{-4}	0.74×10^{-4}	0.16×10^{-4}
600	9.58×10^{-5}	0.25×10^{-4}	0.45×10^{-4}	0.95×10^{-5}
660	7.35×10^{-5}	0.15×10^{-4}	0.23×10^{-4}	0.48×10^{-5}
740	1.28×10^{-5}	0.64×10^{-5}	0.95×10^{-5}	0.19×10^{-5}
820	3.19×10^{-6}	0.32×10^{-5}	0.41×10^{-5}	0.82×10^{-6}
930	3.65×10^{-6}	0.26×10^{-5}	0.15×10^{-5}	0.25×10^{-6}

Table 2: As in Table 1, but for a clustering cone size R=0.7

M_{jj}^{obs}	Systematic uncertainties (%)						Theoretical uncertainties (%)			
	A	B	C	D	E	TOT	F	G	H	TOT
145	12	5	1	16	25	33	6	4	35	36
155	12	5	1	16	25	33	6	4	34	35
165	12	5	1	16	24	32	5	4	33	34
175	12	5	2	16	24	32	5	4	32	33
185	12	6	2	17	23	32	5	4	31	32
195	13	6	2	17	23	32	5	4	30	31
205	13	6	2	17	22	32	5	4	29	30
215	13	6	2	17	22	32	5	4	28	29
225	13	6	2	17	22	32	5	4	27	28
235	13	7	2	17	21	32	5	3	26	27
245	13	7	2	18	21	32	5	3	26	26
255	13	7	3	18	21	32	5	3	25	26
265	14	7	3	18	21	32	5	3	24	25
275	14	7	3	18	21	33	4	3	23	24
285	14	7	3	18	21	33	4	3	23	23
295	14	8	3	19	21	33	4	3	22	23
305	14	8	3	19	21	33	4	3	22	22
315	14	8	4	19	22	34	4	3	21	22
325	14	8	4	19	22	34	4	3	20	21
335	14	8	4	19	22	35	4	3	20	20
345	15	9	4	20	23	35	4	2	19	20
355	15	9	4	20	23	36	4	2	19	19
365	15	9	4	20	23	36	4	2	18	19
375	15	9	5	20	24	37	4	2	18	19
385	15	9	5	21	24	37	3	2	18	18
395	15	9	5	21	25	38	3	2	17	18
410	15	10	5	21	26	39	3	2	17	17
430	15	10	6	22	27	40	3	2	16	16
450	15	10	6	22	28	41	3	2	16	16
480	15	10	7	23	30	43	3	1	15	15
520	16	11	8	24	32	45	2	1	14	14
560	15	11	8	25	34	47	2	1	14	14
600	15	12	9	26	35	49	2	1	14	14
660	15	12	11	28	37	52	2	1	14	14
740	14	13	13	30	39	55	1	1	14	14
820	13	13	16	33	40	58	1	1	14	14
930	11	13	19	37	41	61	1	1	14	14

Table 3: Systematic and theoretical uncertainties for the measurement obtained with a cone radius 1.0: A = 90° crack, B = ϕ crack, C = high energy particle calorimeter response, D = low energy particle calorimeter response, E = fragmentation, F= out of cone losses, G = 30° cut, H = underlying event. A constant uncertainty of 6.8% on the integrated luminosity is also included in the total systematic uncertainty. The theoretical uncertainties due to different structure functions and renormalization scales are not shown.

M_{jj}^{obs}	Systematic uncertainties (%)						Theoretical uncertainties (%)			
	A	B	C	D	E	TOT	F	G	H	TOT
125	11	8	4	14	28	35	25	7	21	34
135	11	8	4	15	28	35	24	6	20	32
145	11	8	4	15	28	35	23	6	20	31
155	12	8	4	15	28	35	22	6	19	30
165	12	8	4	15	28	35	21	5	19	28
175	12	8	4	16	27	35	20	5	18	27
185	12	8	4	16	27	35	19	5	17	26
195	12	8	4	16	27	36	18	4	17	25
205	13	8	4	16	27	36	17	4	16	24
215	13	8	4	17	27	36	16	4	16	23
225	13	9	4	17	27	36	15	4	15	22
235	13	9	4	17	28	37	15	3	15	21
245	13	9	4	17	28	37	14	3	14	20
255	13	9	4	18	28	37	13	3	14	20
265	13	9	4	18	28	37	13	3	14	19
275	14	9	4	18	28	38	12	3	13	18
285	14	9	4	18	28	38	12	2	13	17
295	14	9	4	18	28	38	11	2	13	17
305	14	9	4	19	28	39	11	2	12	16
315	14	9	5	19	28	39	10	2	12	16
325	14	9	5	19	29	39	10	2	12	15
335	14	10	5	19	29	39	9	2	11	15
345	14	10	5	20	29	40	9	1	11	14
355	15	10	5	20	29	40	9	1	11	14
365	15	10	5	20	29	40	8	1	10	13
375	15	10	5	20	29	41	8	1	10	13
385	15	10	5	21	29	41	8	1	10	13
395	15	10	5	21	30	41	7	1	10	12
410	15	10	6	21	30	42	7	1	10	12
430	15	10	6	22	30	42	7	1	9	11
450	15	10	6	22	30	43	7	1	9	11
480	16	11	7	23	31	44	7	1	9	11
520	16	11	7	24	32	45	7	1	8	10
560	16	11	8	25	33	47	7	1	8	10
600	16	12	9	27	34	48	7	1	8	10
660	16	12	10	28	35	51	7	1	8	10
740	15	13	12	31	38	54	7	1	8	10
820	15	13	15	33	40	58	7	1	8	10
930	14	14	18	37	43	63	7	1	8	10

Table 4: As in Table 3, but for a clustering cone size R=0.7

		CONE 1.0			CONE 0.7		
		α_1	α_2	α_3	α_1	α_2	α_3
k	$\gamma_k(M_{jj})$	p_{1k}	p_{2k}	p_{3k}	p_{1k}	p_{2k}	p_{3k}
1	1	1.76	−85.0	7.12	−5.3	−85.0	15.1
2	M_{jj}	1.9×10^{-2}	−0.278	0.148	7.2×10^{-3}	−0.288	0.289
3	M_{jj}^2	1.9×10^{-4}	1.9×10^{-4}	-1.5×10^{-5}	1.55×10^{-4}	2.1×10^{-4}	-1.5×10^{-4}
4	M_{jj}^3	-1.0×10^{-7}	-3.9×10^{-8}	2.1×10^{-8}	-1.1×10^{-7}	-5.8×10^{-8}	9.0×10^{-8}
5	$e^{M_{jj}/350}$	1.81	0	0	3.93	0	0
6	$e^{-M_{jj}/100}$	−7.29	0	0	0	0	0
7	$\sqrt{M_{jj}+100}$	0	8.54	0	0	8.55	0
8	$\sqrt{M_{jj}}$	0	0	−1.84	0	0	−3.79

Table 5: Values of the p_{ik} coefficients and the γ_k functions describing the evolution of the smearing parameters $\alpha_i(M_{jj}) = \sum_k p_{ik}\gamma_k(M_{jj})$. M_{jj} must be given in GeV/c^2 (see text).

	a	b	c	χ^2	Np
Cone 1.0	$(2.50 \pm 0.07) \times 10^{10}$	4.670 ± 0.004	$(5.30 \pm 0.16) \times 10^{-3}$	31.1	37
Cone 0.7	$(4.48 \pm 0.13) \times 10^{9}$	4.424 ± 0.003	$(5.73 \pm 0.15) \times 10^{-3}$	52.3	39

Table 6: CDF fit values for the parameters a, b, c in the parametric expression of the differential cross section $d\sigma/dM_{jj}$: $f(M_{jj}) = aM_{jj}^{-b}e^{-cM_{jj}}$, where M_{jj} is in GeV/c^2 and $f(M_{jj})$ is in nb/(GeV/c^2). The last two columns show the χ^2 and the number of fit points.

	cone 1.0					cone 0.7				
μ^2/p_T^2	4	2	1	.5	.25	4	2	1	.5	.25
DFLM $\Lambda_{QCD} = 160$ MeV	52	43	46	47	52	1	0.3	0.5	0.2	1
DFLM $\Lambda_{QCD} = 260$ MeV	48	50	53	54	50	1	1	1	1	1
DFLM $\Lambda_{QCD} = 360$ MeV	44	47	49	51	50	1	1	1	2	2
DO1	48	49	48	47	47	1	1	1	1	1
DO2	44	46	48	48	48	1	1	1	2	2
EHLQ1	36	37	38	40	40	0.04	0.2	0.3	0.3	0.2
EHLQ2	19	21	23	25	25	0.001	0.001	0.1	0.04	0.1
HMRSB	45	45	47	46	45	1	1	1	1	2
HMRSE	45	43	40	37	33	3	3	3	3	3
MT E1	56	57	57	56	56	2	1	1	2	2
MT B2	63	63	64	64	64	4	5	4	5	5
MT B1	57	57	59	59	59	2	2	2	2	2
MT S1	57	57	58	58	58	2	2	2	2	2

Table 7: Confidence levels (%) of LO QCD for various structure functions including EHLQ and DO for backward compatibility with older calculations.

	cone 1.0		cone 0.7	
A	1	.5	1	.5
HMRSB	58	57	3.6	4.6
MT S1	69	66	6.9	6.5

Table 8: Confidence levels (%) of NLO QCD for two structure functions.

Figure Captions.

Fig. 1: Observed dijet mass spectrum for a cone size R=1, integrated over the pseudorapidity intervals $|\eta_1|, |\eta_2| < 0.7$. The measurement is compared on absolute scale with theoretical predictions modified to take into account the detector effects. The band defined by the two solid lines is the envelope of different LO QCD predictions obtained by varying the renormalization scale ($p_T/2 < \mu < 2p_T$) and the structure function parametrization. The dotted line shows one NLO prediction obtained using the structure function HMRSB and the renormalization scale $\mu = 0.5 M_{jj}/2cosh(0.7\eta^*)$. The error bars on the data represent statistical and M_{jj}-dependent systematic errors combined in quadrature. An overall normalization uncertainty is also indicated.

Fig. 2: As in Fig. 1, but for a clustering cone size R=0.7.

Fig. 3: $(d\sigma_{R=1}/dM_{jj}^{obs})/(d\sigma_{R=0.7}/dM_{jj}^{obs})$ as a function of M_{jj}. The error bars on the data points represent the statistical and systematic errors added in quadrature. Bin to bin correlations are not shown. The NLO predictions are shown for the two structure functions HMRSB and MTS1 and for the renormalization scales $\mu = AM_{jj}/2cosh(0.7\eta^*)$ where A=0.25 (dotted lines), A=0.5 (solid lines) and A=1 (dashed lines).

Fig. 4: The M_{jj} spectra for (a) R=1 and (b) R=0.7 compared to the best fit using the quantity $(data - fit)/fit$. The best fit, used as a reference (horizontal line), is the parametric function $f(M_{jj}) = aM_{jj}^{-b}e^{-cM_{jj}}$ folded with the detector resolution. Errors are statistical. The deviations from the best fit, $(QCD - fit)/fit$, of LO (solid

lines) and NLO (dotted lines) theoretical predictions are also shown for the MTS1 structure function and varying choices of renormalization scale as in Tables 7 and 8. All the theories have been folded with the appropriate detector resolution and fit to the data by freely varying the normalization factor.

Fig. 5: As in Fig. 3, but LO and NLO predictions are obtained using the structure function HMRSB.

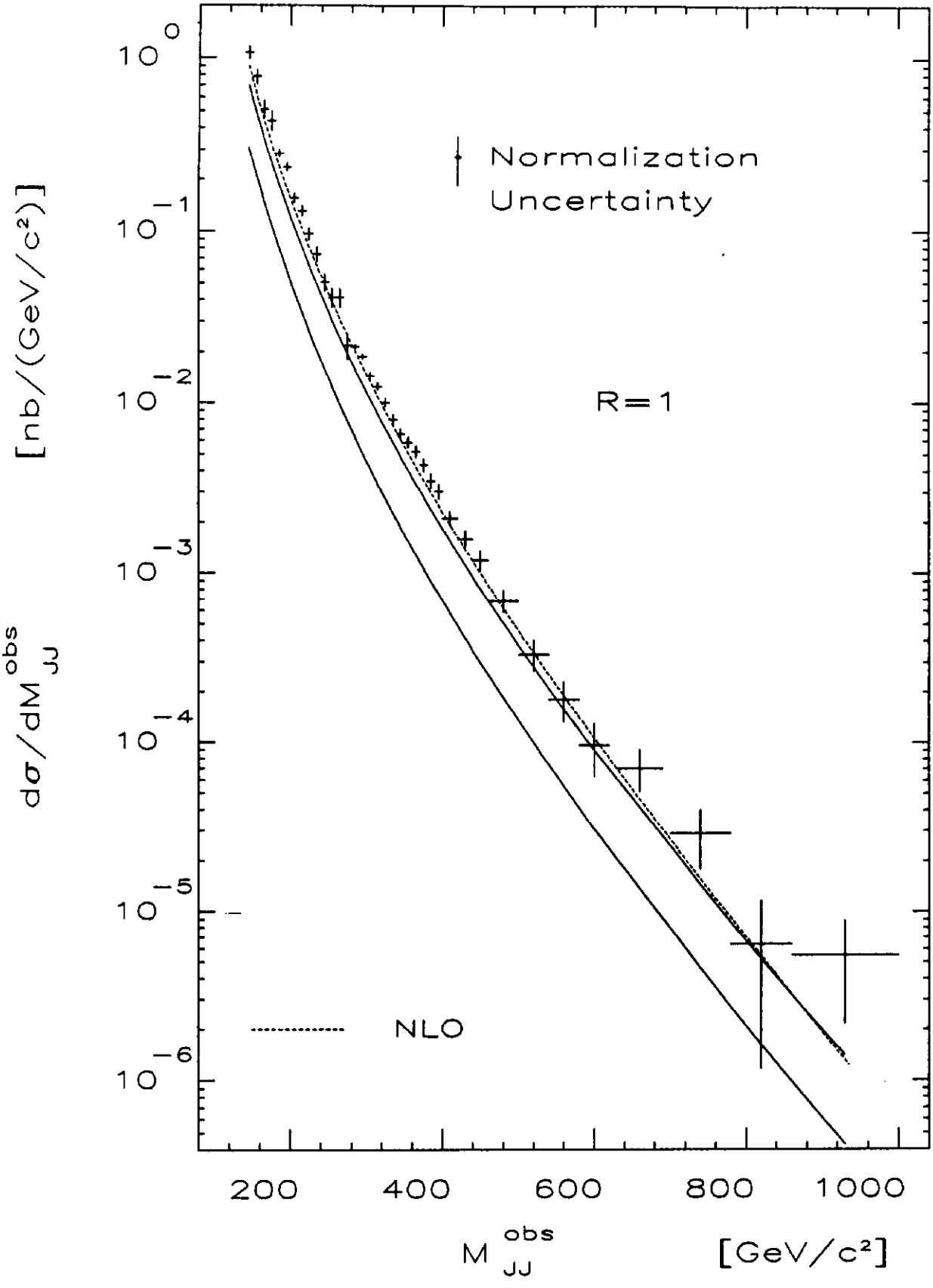
Normalization
Uncertainty
R=1
NLO
$d\sigma/dM_{JJ}^{obs}$ [nb/(GeV/c²)]
M_{JJ}^{obs} [GeV/c²]
10^{0}
10^{-1}
10^{-2}
10^{-3}
10^{-4}
10^{-5}
10^{-6}
200
400
600
800
1000

FIG. 1

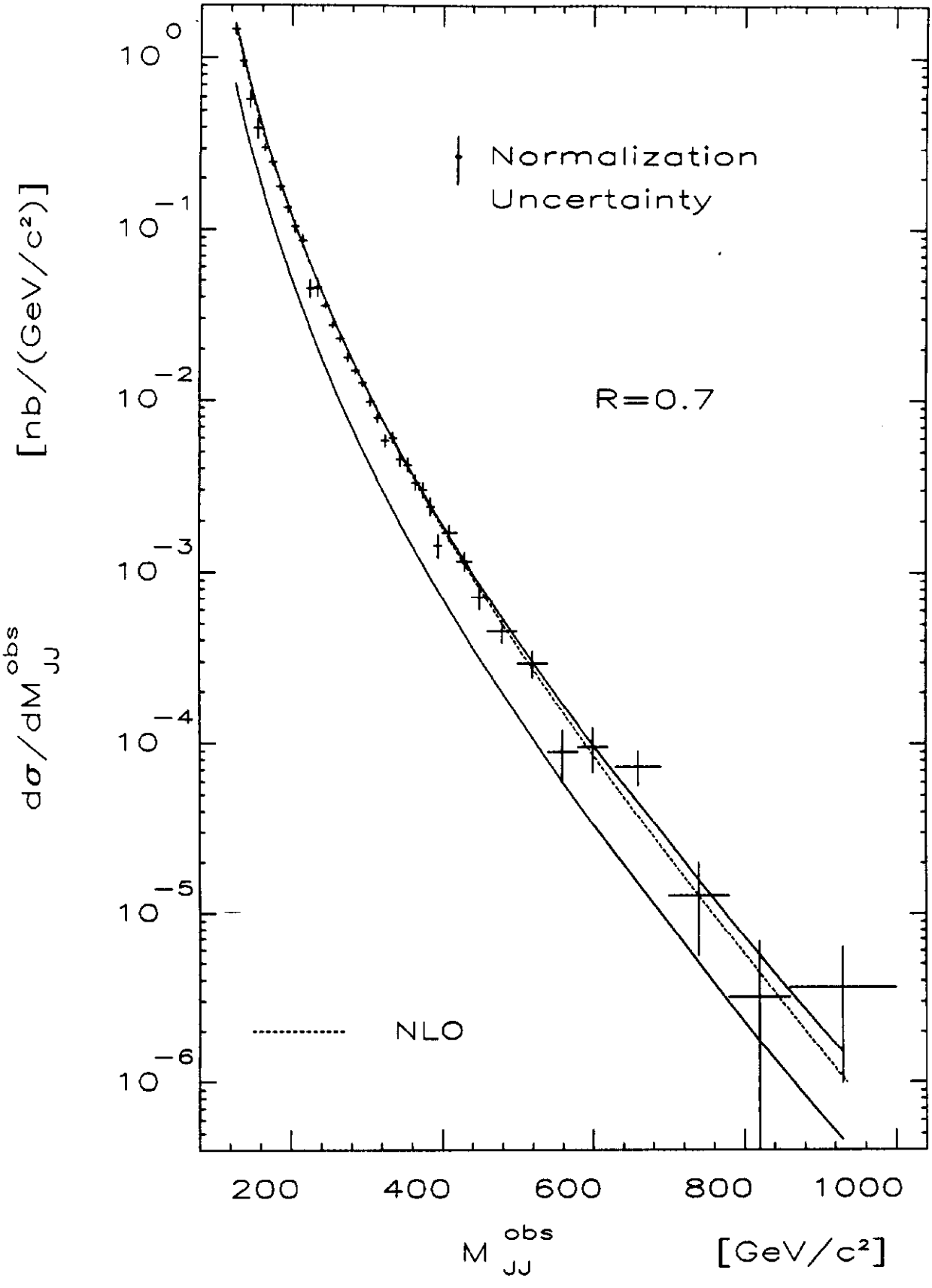
Normalization
Uncertainty
R=0.7
NLO
$d\sigma/dM_{JJ}^{obs}$ [nb/(GeV/c²)]
M_{JJ}^{obs} [GeV/c²]
10^{0}
10^{-1}
10^{-2}
10^{-3}
10^{-4}
10^{-5}
10^{-6}
200
400
600
800
1000

FIG. 2

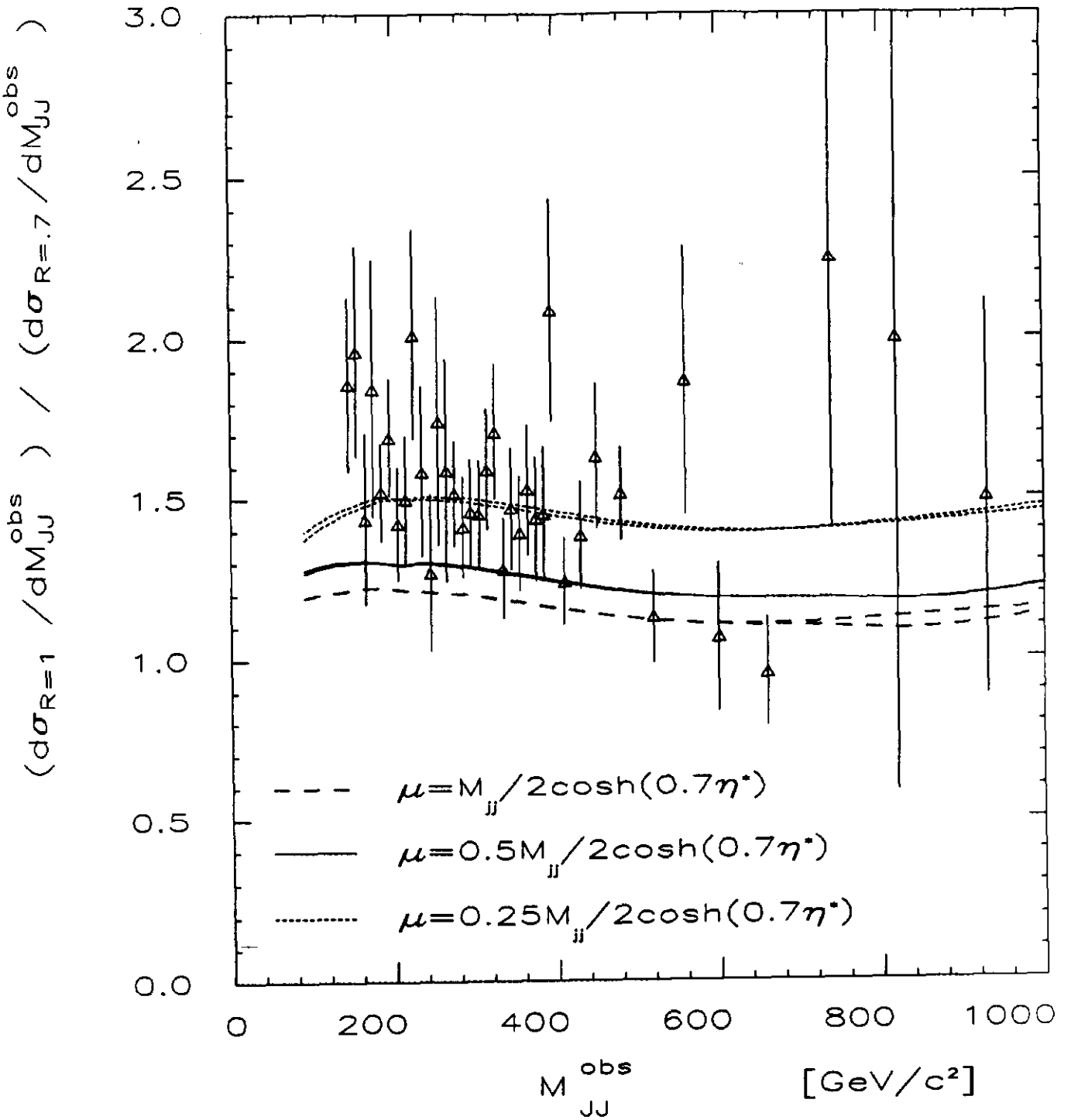
3.0
2.5
2.0
1.5
1.0
0.5
0.0
0
200
400
600
800
1000
$(d\sigma_{R=1}/dM_{JJ}^{obs}) / (d\sigma_{R=.7}/dM_{JJ}^{obs})$
M_{JJ}^{obs} [GeV/c²]
$\mu=M_{jj}/2\cosh(0.7\eta^*)$
$\mu=0.5M_{jj}/2\cosh(0.7\eta^*)$
$\mu=0.25M_{jj}/2\cosh(0.7\eta^*)$

FIG. 3

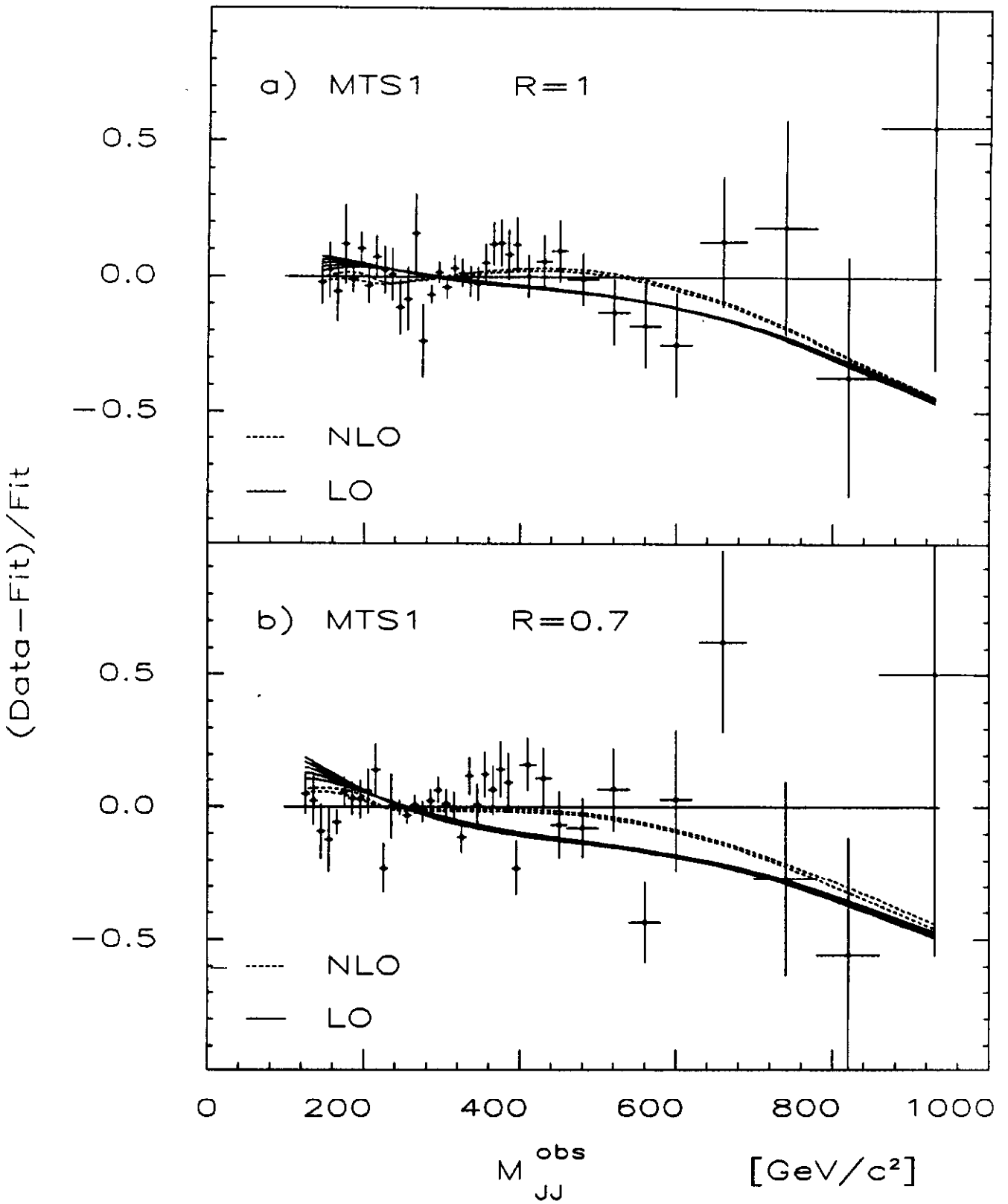
a) MTS1 R=1
b) MTS1 R=0.7
NLO
LO
NLO
LO
0.5
0.0
−0.5
0.5
0.0
−0.5
(Data−Fit)/Fit
0
200
400
600
800
1000
M JJ obs
[GeV/c²]

FIG. 4

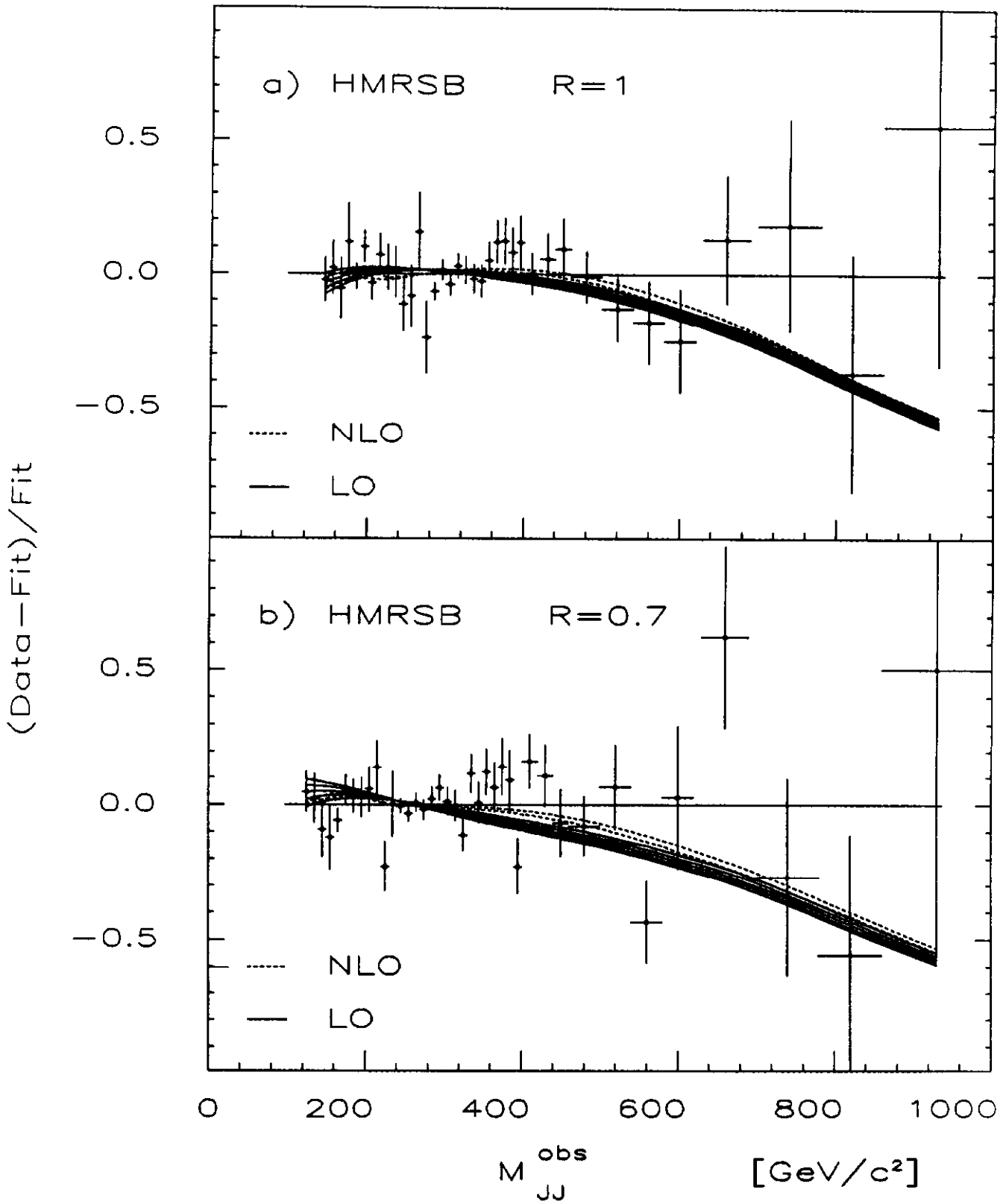
a) HMRSB R=1
0.5
0.0
−0.5
NLO
LO
b) HMRSB R=0.7
0.5
0.0
−0.5
NLO
LO
(Data−Fit)/Fit
0
200
400
600
800
1000
M JJ obs
[GeV/c²]

FIG. 5